

# Unveiling the Interaction Mechanisms of Electron and X-ray Radiation with Halide Perovskite Semiconductors using Scanning Nanoprobe Diffraction

Jordi Ferrer Orri, Tiarnan A.S. Doherty, Duncan Johnstone, Sean M. Collins, Hugh Simons, Paul A. Midgley, Caterina Ducati,\* and Samuel D. Stranks\*

The interaction of high-energy electrons and X-ray photons with beam-sensitive semiconductors such as halide perovskites is essential for the characterization and understanding of these optoelectronic materials. Using nanoprobe diffraction techniques, which can investigate physical properties on the nanoscale, studies of the interaction of electron and X-ray radiation with state-of-the-art  $(\text{FA}_{0.79}\text{MA}_{0.16}\text{Cs}_{0.05})\text{Pb}(\text{I}_{0.83}\text{Br}_{0.17})_3$  hybrid halide perovskite films (FA, formamidinium; MA, methylammonium) are performed, tracking the changes in the local crystal structure as a function of fluence using scanning electron diffraction and synchrotron nano X-ray diffraction techniques. Perovskite grains are identified, from which additional reflections, corresponding to  $\text{PbBr}_2$ , appear as a crystalline degradation phase after fluences of  $200 \text{ e}^- \text{ \AA}^{-2}$ . These changes are concomitant with the formation of small  $\text{PbI}_2$  crystallites at the adjacent high-angle grain boundaries, with the formation of pinholes, and with a phase transition from tetragonal to cubic. A similar degradation pathway is caused by photon irradiation in nano-X-ray diffraction, suggesting common underlying mechanisms. This approach explores the radiation limits of these materials and provides a description of the degradation pathways on the nanoscale. Addressing high-angle grain boundaries will be critical for the further improvement of halide polycrystalline film stability, especially for applications vulnerable to high-energy radiation such as space photovoltaics.

## 1. Introduction

Halide perovskite materials exhibit promising characteristics for optoelectronics applications. These materials can be fabricated through facile processing techniques and yield high performance devices, albeit with large compositional and structural heterogeneities at multiple length scales.<sup>[1]</sup> Heterogeneity, particularly on the nano- and microscale, is key to understanding some of the critical questions on performance and stability.<sup>[1–3]</sup> Scanning nanoprobe characterization techniques, such as scanning electron diffraction (SED) or nanoprobe X-ray diffraction (nXRD), are particularly advantageous as they can access both the relevant nano- and microscales.<sup>[4,5]</sup>

Both techniques use focused radiation, which interacts with the material and can impact its structure and chemistry, especially for materials with complex stoichiometries such as hybrid halide perovskites that mix organic and inorganic ions. These hybrid halide perovskites are

J. Ferrer Orri, T. A.S. Doherty, S. D. Stranks  
Cavendish Laboratory  
University of Cambridge  
Cambridge CB3 0HE, UK  
E-mail: sds65@cam.ac.uk

J. Ferrer Orri, D. Johnstone, P. A. Midgley, C. Ducati  
Department of Materials Science and Metallurgy  
University of Cambridge  
Cambridge CB3 0FS, UK  
E-mail: cd251@cam.ac.uk

 The ORCID identification number(s) for the author(s) of this article can be found under <https://doi.org/10.1002/adma.202200383>.

© 2022 The Authors. Advanced Materials published by Wiley-VCH GmbH. This is an open access article under the terms of the Creative Commons Attribution License, which permits use, distribution and reproduction in any medium, provided the original work is properly cited.

DOI: 10.1002/adma.202200383

S. M. Collins  
School of Chemical and Process Engineering & School of Chemistry  
University of Leeds  
Leeds LS2 9JT, UK

H. Simons  
Department of Physics  
Technical University of Denmark  
Copenhagen 2800, Denmark

S. D. Stranks  
Department of Chemical Engineering and Biotechnology  
University of Cambridge  
Cambridge CB3 0AS, UK

uniquely promising light-weight candidates for space photovoltaic applications, with reports showing excellent radiation hardness under extreme space conditions of proton and electron exposure.<sup>[6–8]</sup> Large fluxes of high-energy particles, such as trapped electrons in orbit extending up to 1 MeV energies, can trigger defect generation and degradation of these materials, in similar ways to the degradation induced during characterization techniques.<sup>[9,10]</sup> Based on studies reporting radiation damage of hybrid perovskite being dependent on the total dose rather than on the dose rate,<sup>[11,12]</sup> microscopy techniques such as SED and nXRD may be used to mimic large total radiation exposures while characterizing defect generation and degradation in vacuum.

Understanding the interaction of the high-energy probe with the samples is critical for acquisition, data analysis, and detector applications. For example, the interaction of focused electron beams with halide perovskites has been reviewed and can be quantified with critical radiation values. These critical values are defined as particle fluences (in units of particles  $\text{\AA}^{-2}$ ) representing the rate of characteristic irreversible structural changes under particle exposure.<sup>[12–14]</sup> For halide perovskites, e.g., higher acceleration voltages increase these critical values by reducing the cross-section for beam-specimen interaction, while the use of cryogenic temperatures induces rapid amorphization and reduces these values.<sup>[11,14]</sup> Rothmann et al. used transmission electron microscopy (TEM) to quantify structural changes in methylammonium lead iodide films ( $\text{MAPbI}_3$ ) at fluences as low as  $100 \text{ e}^- \text{\AA}^{-2}$ ,<sup>[11]</sup> in which loss of the organic moieties results in lattice contraction and the formation of a supercell, further described by Chen et al. as  $\text{MAPbI}_{2.5}$ , ultimately degrading into  $\text{PbI}_2$ .<sup>[15,16]</sup> The appearance of an intermediate phase of degradation agrees with similar studies by scanning electron microscopy techniques.<sup>[17–19]</sup> Alberti et al. also reported the detrimental effect of having excess Pb-related defects during fabrication, which aggregate and feed degradation at grain boundaries upon electron irradiation.<sup>[20]</sup> However,  $\text{Pb}^0$  formation is usually observed as a degradation product of fully inorganic compositions, such as  $\text{CsPbI}_3$ , upon electron irradiation. This is because the inorganic cation is less prone to be reduced than its organic counterparts or than the Pb cation.<sup>[21,22]</sup>

Moving beyond the workhorse hybrid  $\text{MAPbI}_3$  composition, Rothmann et al. recently reported high-resolution scanning transmission electron microscopy (STEM) images of evaporated formamidinium lead iodide ( $\text{FAPbI}_3$ ) thin films, reporting the appearance of additional reflections at low fluences of  $200 \text{ e}^- \text{\AA}^{-2}$ , the loss of the perovskite phase at  $600 \text{ e}^- \text{\AA}^{-2}$ , and the eventual formation of  $\text{PbI}_2$  grown on the lattice-expanded degraded phase of  $\text{FAPbI}_3$  after  $1000 \text{ e}^- \text{\AA}^{-2}$ .<sup>[23]</sup>

The effect of scanning X-ray probes on halide perovskites, on the other hand, has been less studied than for electron microscopy.<sup>[5]</sup> The critical fluences for  $\text{MAPbI}_3/\text{MAPbBr}_3$  derivatives vary for different microscopy techniques. The nano-X-ray beam-induced current signal is highly sensitive to defects and was rapidly affected at the lowest fluences of  $10^3$  photons  $\text{\AA}^{-2}$ .<sup>[24]</sup> Nano-X-ray diffraction (nXRD) and fluorescence (nXRF) were found to withstand 10x higher exposures, since these signals are more intense, generated by larger volumes, and easier to record.<sup>[25,26]</sup> Li et al. reported similar critical fluences of  $10^2$

and  $10^4$  photons  $\text{\AA}^{-2}$  for  $\text{MAPbBr}_3$  and  $\text{CsPbBr}_3$  single crystals, respectively, yet the appearance of additional phases was not reported at these fluences.<sup>[25]</sup> Other studies have reported comparable XRD signal decays due to loss of crystallinity after long X-ray exposures.<sup>[27]</sup> These studies, specifically identifying the effect of synchrotron scanning probes on the material, are not to be confused with the plethora of laboratory XRD reports elucidating the degradation products of halide perovskites at millimeter scale due to external factors such as light, air, temperature, or passivating agents.<sup>[28–30]</sup>

While the majority of the work related to beam damage has been performed on  $\text{MAPbI}_3$ , state-of-the-art halide perovskites are FA-rich mixed-cation mixed-halide compositions, especially those relevant for tandem and space photovoltaic applications.<sup>[31,32]</sup> Such compositions exhibit distinct chemical and structural degradation pathways, yet no comprehensive studies on such systems have been reported to date. Rigorously establishing the radiation effects on these more complex compositions to allow elucidation of global mechanisms, as well as obtaining insight into the role of grain boundaries and complicated junctions, is of immense interest.

Here, we use two advanced nanoprobe diffraction techniques, SED and nXRD, to understand the respective interaction of 200 keV electrons and 20 keV X-rays with the local nanostructure of solution-processed halide perovskite films of triple-cation nominal composition  $(\text{FA}_{0.79}\text{MA}_{0.16}\text{Cs}_{0.05})\text{Pb}(\text{I}_{0.83}\text{Br}_{0.17})_3$ .<sup>[33]</sup> By using low-dose diffraction microscopy, we can spatially resolve the diffraction information on the nanoscale as a function of radiation exposure. The use of finely tunable acquisition conditions allows us to track the compositional and structural evolution of degradation processes of hybrid perovskite films, as well as their spatial origin. We show that change is predominantly observed at specific sites in the polycrystalline film which are more defective and evolve toward new structures over time, such as  $\text{PbI}_2$  and  $\text{PbBr}_2$  formation. Specifically, high-angle grain boundaries in the polycrystalline structure trigger such changes to the nanostructure. These studies establish critical radiation values and interaction mechanisms of electron and X-ray radiation for mixed-cation mixed-halide perovskites, allowing the elucidation of global mechanisms for degradation, as well as stability windows in both measurement and application of these radiation types.

## 2. Results and Discussion

Thin films of  $(\text{FA}_{0.79}\text{MA}_{0.16}\text{Cs}_{0.05})\text{Pb}(\text{I}_{0.83}\text{Br}_{0.17})_3$  were solution-processed following optimized protocols for device fabrication compatible with silicon nitride (SiN) grids, ensuring reproducible and comparable results to high-performance devices prepared on standard substrates,<sup>[34]</sup> while also enabling the use of transmission microscopy techniques. 5D datasets of the films were acquired by combining a time series ( $t$ ) of SED frames. Each SED frame was acquired over the same region of the sample ( $x, y$ ), wherein each scanned position contains an electron diffraction pattern ( $k_x, k_y$ ). Between each frame, the electron beam was digitally driven to a controlled beam-parking position within the field of view before being blanked, labeled with a cross in **Figure 1**. Visible beam-induced accelerated changes are

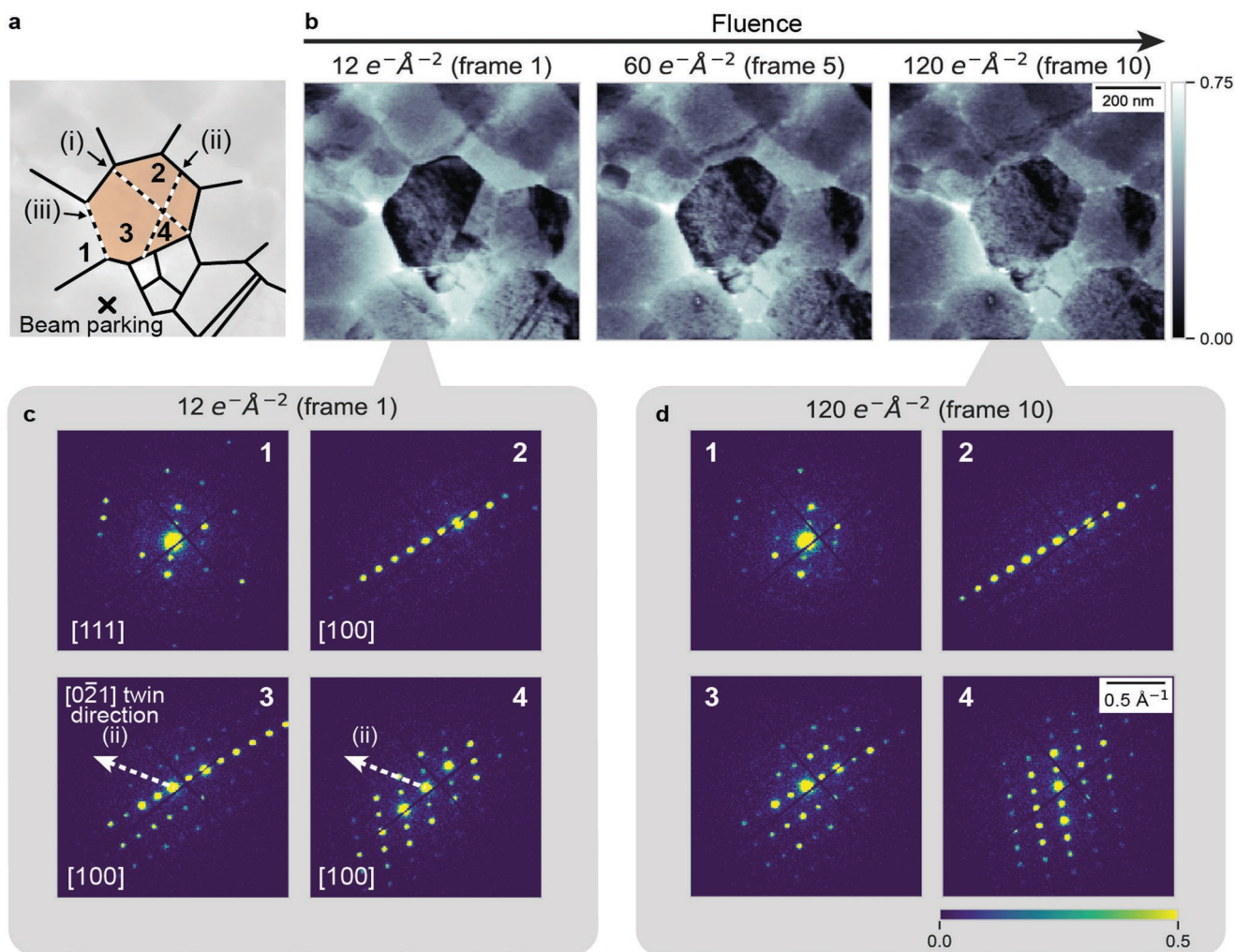


**Figure 1.** Visualizing grain boundary types and their evolution under low electron exposure using scanning electron diffraction (SED) on  $(\text{FA}_{0.79}\text{MA}_{0.16}\text{CS}_{0.05})\text{Pb}(\text{I}_{0.83}\text{Br}_{0.17})_3$  halide perovskite films. a) Schematic of the perovskite grain showing the areas of interest from which diffraction patterns are extracted (in Arabic numerals), and three interfaces between crystallographic domains indicated by dashed lines (in Roman numerals): i) grain bending across regions 2 and 3, ii) a twin grain boundary at the  $(0\bar{2}1)$  plane between regions 3 and 4, and iii) a high-angle grain boundary interphasing two grains at different zone axes between regions 1 and 3. The beam-parking position is labeled with a cross. b) Evolution of vBF images of a perovskite film for up to  $120 \text{ e}^- \text{ \AA}^{-2}$  fluence. c) The resulting averaged diffraction pattern for four different areas at the 1st frame ( $12 \text{ e}^- \text{ \AA}^{-2}$ ) and d) at the 10th frame ( $120 \text{ e}^- \text{ \AA}^{-2}$ ). Regions denoted with numerals in (a) correspond to the diffraction in (b) and (c). All intensity scale bars correspond to the normalized vBF and the diffraction intensity.

observed in the vicinity of the beam-parking position, within a radius of  $\approx 90 \text{ nm}$ , equivalent to the radius of the interaction volume (see Figure S1, Supporting Information). The circular area around the beam parking position is disregarded, using the rest of the scan area for this study, only irradiated during beam rastering.

The rich diffraction-based multidimensional dataset enables the investigation of the effects of cumulative electron beam exposure on the nanoscale. Repeated scans were acquired at total fluences from  $12 \text{ e}^- \text{ \AA}^{-2}$  (1 frame) up to  $900 \text{ e}^- \text{ \AA}^{-2}$  (75 frames), at which point the diffraction from the halide perovskite film had substantially degraded. Figure 1 shows the evolution of the local nanoscale diffraction of a representative perovskite grain at low electron exposure, up to a cumulative fluence of  $120 \text{ e}^- \text{ \AA}^{-2}$  corresponding to the first 10 frames.

The term grain is used here as the apparent area delimited by morphological grain boundary features observed in the electron microscope.<sup>[35,36]</sup> For each diffraction pattern, electrons at low scattering angle (the direct beam) are collected at the origin, which is surrounded by a series of diffraction peaks corresponding to scattering vectors near or at the Bragg condition. We create virtual bright-field images (vBF) of the scanned region by mapping the intensity of the direct beam below a virtual aperture of radius  $4 \times 10^{-3} \text{ \AA}^{-1}$  (semi-angle of detector of  $2.39 \text{ mrad}$ ), as a function of the probe position. Virtual dark-field images (vDF) can be created by mapping the intensity of selected scattered signals, corresponding to a fixed virtual aperture size and position in reciprocal space within  $1.18 \text{ \AA}^{-1}$  range ( $70.3 \text{ mrad}$ , see Figure S2, Supporting Information). The vBF images mostly contain information from the nonscattered

beam and low-angle inelastic scattering, resulting in relatively lower intensities when the sample is at a strongly diffracting orientation or where it is thicker.

The grain labeled in Figure 1a exhibits intense diffraction as its constituent orientations match a low-angle zone axis and is thus selected for detailed study. The vBF images in Figure 1b reveal the polycrystalline nature of the perovskite film, as well as heterogeneity in the diffraction contrast within each grain. These variations in contrast are a result of chemical and structural heterogeneity on the nanoscale.<sup>[1,37]</sup> To illustrate the difference between individual grains, diffraction patterns are obtained by summing pixels within the grain at the center of the region of interest, denoted by Arabic numerals in Figure 1a. The diffraction patterns at the near-pristine state are shown in Figure 1c, acquired at the lowest electron fluence of  $12 \text{ e}^- \text{ \AA}^{-2}$  (first frame).

All diffraction patterns can be indexed to a tetragonal perovskite structure in the  $P4/mbm$  space group with lattice parameters of  $a = b = 9.00$  and  $c = 6.36 \text{ \AA}$ ,<sup>[38]</sup> each near the  $[100]$  zone axis with slightly different crystal tilt relative to the electron beam (see Figures S3–S5 in the Supporting Information for simulated diffraction pattern matching experimental diffraction). At least three different crystal orientations can be observed within this grain in this scattering geometry. The interfaces between crystallographic domains can be identified in the virtual images and labeled by dashed lines and Roman numerals in the schematic (also see Figure S6, Supporting Information). Grain bending due to the soft perovskite lattice is observed in (i), across the upper and the lower parts of the central grain in Figure 1b (region 2 and 3, respectively). The difference between their diffraction patterns can be attributed to small in-plane crystal tilt of  $\approx 2^\circ$  (see Figure S7, Supporting Information). When sudden changes in crystal orientation are observed, different types of grain boundaries can be identified.<sup>[39]</sup> In (ii) a twin boundary, a special case of a large angle grain boundary for which there is no atomic misfit, is observed between the regions 3 and 4 in Figure 1b. Detailed analysis of the diffraction pattern shows the lattice being mirrored across the  $(0\bar{2}1)$  plane, marked with a dashed line. Distinctly, the grain boundaries around the central grain are iii) high-angle, as inferred from orientation analysis on the adjacent grains being near the  $[111]$  zone axis instead (see Figure 1b,c region 1, for the diffraction pattern of an adjacent grain). The nature of these two types of grain boundary is discussed in more detail later.

The evolution of the diffraction patterns in Figure 1, after  $120 \text{ e}^- \text{ \AA}^{-2}$  of accumulated fluence (10 frames), reveals that the strong diffraction contrast seen in the vBF images rapidly becomes more homogenous. The diffraction patterns at the 1st and 10th frames show a small relative tilt of the order of a few degrees toward alignment to the  $[100]$  zone axis. We attribute these tilts to microstructural changes on the nanoscale, noting that bending of the support membrane cannot be excluded. This tilting is visible in the regions labeled as 3 and 4 in Figure 1c, showing more evenly distributed diffraction spots near the center of the beam after 10 scans. These tilts are not observable in the region labeled as 2, where the diffraction pattern, originally off the zone axis by a larger tilt, would need to rotate by larger angles to get toward the zone axis. These observations suggest that changes in the perovskite microstruc-

ture may already start at extremely low electron exposure of tens of  $\text{e}^- \text{ \AA}^{-2}$ . These fluences are sufficient to provide enough energy to modify the pristine grain orientation without measurable lattice distortions (see Figures S7 and S8 in the Supporting Information for a more detailed evolution at low fluences of these diffraction patterns). Similar changes in the tilt of grains, commonly seen in thin polycrystalline films deposited on TEM substrates, are observed from the diffraction patterns in most of the grains in the scanned region, as well as in other SED experiments taken from other halide perovskite films of the same composition (see Figure S9, Supporting Information).

We now consider further electron exposure by taking cumulative fluences up to  $240 \text{ e}^- \text{ \AA}^{-2}$ , as shown in Figure 2a. The evolution of vBF contrast beyond  $240 \text{ e}^- \text{ \AA}^{-2}$  fluence suggests the formation of pinholes at the high-angle grain boundaries (Figure 2b). Degradation at the grain boundaries can be attributed to the loss of chemical species and lattice contraction due to the transformation from pristine perovskite to lead halide degradation products (see Figure S10 in the Supporting Information for the histograms of the Pb–Pb distances for the perovskite structure, and some of the lead halide structures with shorter Pb–Pb distances). Similar observations have been reported in TEM mode.<sup>[11]</sup> Overall, there is a constant decrease in the total intensity of the vBF images by  $\approx 25\%$  that occurs uniformly across the whole scanned area over  $240 \text{ e}^- \text{ \AA}^{-2}$  (20 frames), seen in Figure 1b. Further electron exposure results in roughening of the grain and a decrease of the total scattering intensity by  $\approx 50\%$  after  $480 \text{ e}^- \text{ \AA}^{-2}$  (40 scans), seen in Figure 2b. We note that such a large change in the vBF intensity cannot be attributed to fluctuations of the electron emission gun alone (Figure S11, Supporting Information). The loss of intensity of the direct beam could be attributed to the sample thickening by deposition of an amorphous carbon layer on the surface (see the Supporting Information), and to possible densification of the perovskite structure by amorphization or the loss of the lighter elements such as the organic cations. These changes would increase scattering, as seen in the virtual images created from the annularly integrated vDF (Figure S11, Supporting Information).

We now inspect how the diffraction patterns near the  $[100]$  zone axis, taken from the central grain, change in Figure 2c. Weak Bragg reflections emerge from region 1 in the grain in Figure 2a after  $240 \text{ e}^- \text{ \AA}^{-2}$  (20 frames). These additional reflections, marked with white arrows, cannot be indexed to the pristine perovskite structure at  $\vec{k} = 0.23, 0.34, \text{ and } 0.47 \text{ \AA}^{-1}$ . Close assessment reveals that the patterns from this region are indexable to  $\text{PbBr}_2$  at the  $[111]$  zone axis within a  $0.01 \text{ \AA}^{-1}$  error, as shown in Figure 2d. This suggests the presence of these lead halide species epitaxially growing on the perovskite grain. We ruled out the possibility of this being due to superlattice reflections from the orthorhombic  $Pnma$  space group structure at the  $[001]$  zone axis, since the reflections are not located at the expected  $\frac{1}{2}(hkl)$  positions (see indexation in Figure S3, Supporting Information).<sup>[15,40]</sup>

In contrast, a diffraction pattern taken from region 2 in Figure 2a after  $480 \text{ e}^- \text{ \AA}^{-2}$  exposure (40 frames) shows diffuse diffraction, attributed to the amorphous SiN substrate or amorphization of the perovskite crystal. Weak diffraction reflections at  $\vec{k} = 0.26, 0.24, \text{ and } 0.26 \text{ \AA}^{-1}$  are also visible. These

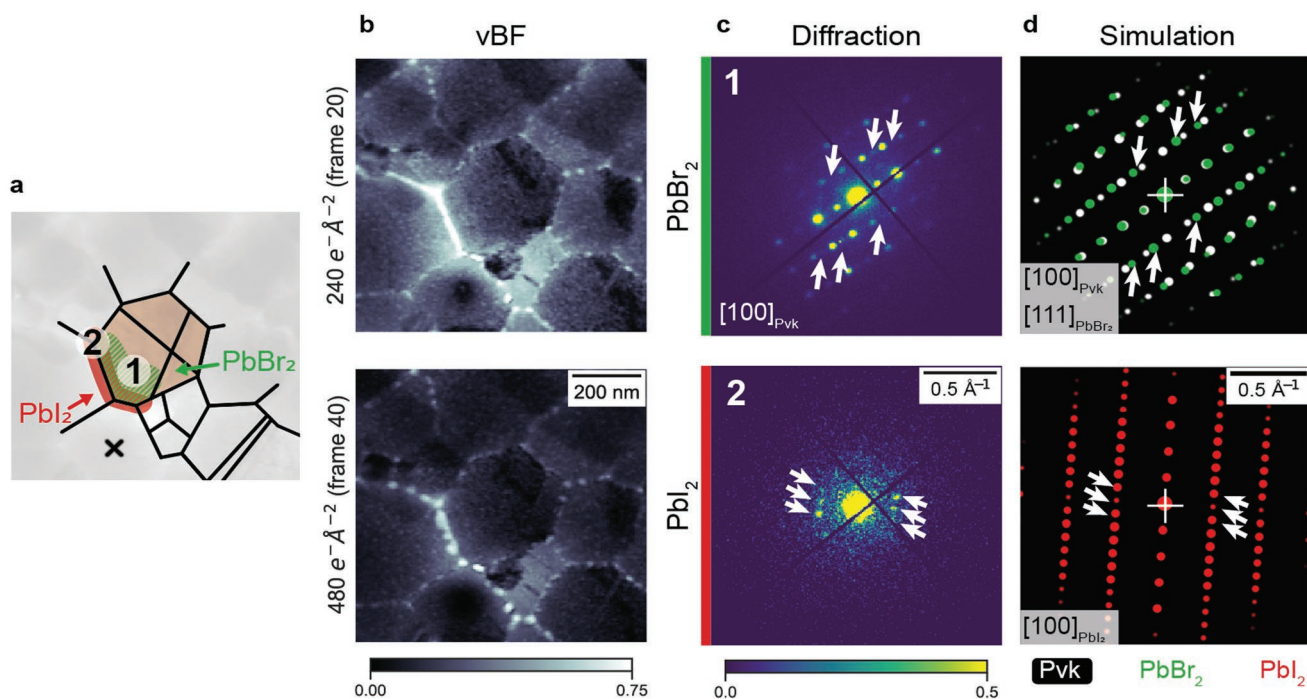


**Figure 2.** Probing the emergence of lead halide species on the nanostructure of  $(\text{FA}_{0.79}\text{MA}_{0.16}\text{Cs}_{0.05})\text{Pb}(\text{I}_{0.83}\text{Br}_{0.17})_3$  halide perovskite films at high electron exposure using SED. a) Schematic of the perovskite grain showing the areas of interest from which  $\text{PbI}_2$  and  $\text{PbBr}_2$  species are observed and from which diffraction patterns are extracted, labeled as 1 and 2, respectively. b) The vBF images at the 20th and 40th frames. c) For each frame, a normalized diffraction pattern from the labeled region is shown. Some additional diffraction spots, marked with white arrows, are observed: the extra reflections in region 1 can be indexed to  $\text{PbBr}_2$  near the  $[111]$  zone axis, and the extra reflections in region 2 can be indexed to  $\text{PbI}_2$  near the  $[100]$  zone axis. d) Simulated patterns for the perovskite (Pvk), the  $\text{PbBr}_2$  and the  $\text{PbI}_2$  phases in white, green and red, respectively. The diffraction patterns computed using CrystalMaker match those seen experimentally.

reflections are indexable to the  $(011)$ ,  $(010)$ , and  $(01\bar{1})$  peaks of  $\text{PbI}_2$  at the  $[\bar{1}00]$  zone axis within  $0.01 \text{\AA}^{-1}$  error, as shown in Figure 2d.  $\text{PbI}_2$  can form by stacking  $\text{PbI}_2$  layers in many possible ways, resulting in different polytypes.<sup>[41]</sup> We note the reflections observed here suggest the formation of the 4H polytype, in contrast to other polytypes such as 2H or 6H reported in other studies.<sup>[20,23]</sup> Despite some ambiguity in classifying the exact  $\text{PbI}_2$  polytype in literature, these phases are remarkably similar and the formation of small precipitates of  $\text{PbI}_2$  is unambiguously observed (see indexation in Figure S5, Supporting Information).<sup>[41]</sup>

To further understand the evolution of phases in Figure 2, we use SED to spatially map the crystallographic changes. Figure 3 shows the evolution of the vDF images created for the perovskite  $(00\bar{2})$  reflection, the  $(211)$   $\text{PbBr}_2$  reflection, and the  $(011)$   $\text{PbI}_2$  reflection (Figure 3a). While the vDF image intensity for the perovskite diffraction peak fades upon exposure, the vDF images of the additional reflections can spatially pinpoint the origin of these changes (Figure 3b). The lead halides appear to be spatially anticorrelated: epitaxial 4H- $\text{PbI}_2$  precipitates grow at the grain boundary and the  $\text{PbBr}_2$  reflections appear at the opposite side of the boundary within the perovskite grain. At extreme cumulative fluences of  $>480 \text{e}^- \text{\AA}^{-2}$  (40 frames), most diffraction from crystalline species has faded, so the vDF images are dominated by diffuse scattering and noise, especially for diffraction spots near the direct beam. At these high fluences, the  $\text{PbI}_2$  diffraction features remain more visible

than the  $\text{PbBr}_2$ , possibly attributed to the bromine precipitates moving away from the zone axis. Some additional vDF images of  $\text{PbI}_2$  precipitates forming at the grain boundaries are identified in Figures S12 and S13 in the Supporting Information, though we note that any  $\text{PbI}_2$  trace crystallites that are too small may be undetectable in SED. The  $\text{PbI}_2$  features are extremely local, only detectable across a few scanned pixels ( $\approx 5\text{--}30 \text{nm}$ ). Moreover, some  $\text{PbI}_2$  features appear near diffraction spots attributed to the perovskite phase, creating noisy features in the vDF images at the early scans.

These changes are local to the bottom-left corner of the grain, suggesting that lead halides nucleate nonuniformly across the grain. Perovskite samples of similar compositions have been reported to show compositional heterogeneity across grains, with Br-rich clusters at the grain boundaries.<sup>[42,43]</sup> Based on the homogeneity of the diffraction pattern across the grain in the pristine state of the film, chemical heterogeneity must be small, yet present enough to help drive the reported local changes. Distinctively, degradation does not appear to originate from the twin boundaries, consistent with theoretical predictions, whereby the octahedron face-sharing present at the twin boundary stabilizes the twins.<sup>[44,45]</sup> Therefore, not all defects affect degradation in the same way.

Intensity profiles for the perovskite  $(00\bar{2})$ , the  $(211)$   $\text{PbBr}_2$ , and the  $(011)_2$  reflections are plotted in Figure 3c. These profiles suggest that the critical fluence for this mixed cation composition, the fluence at which the original diffraction intensity

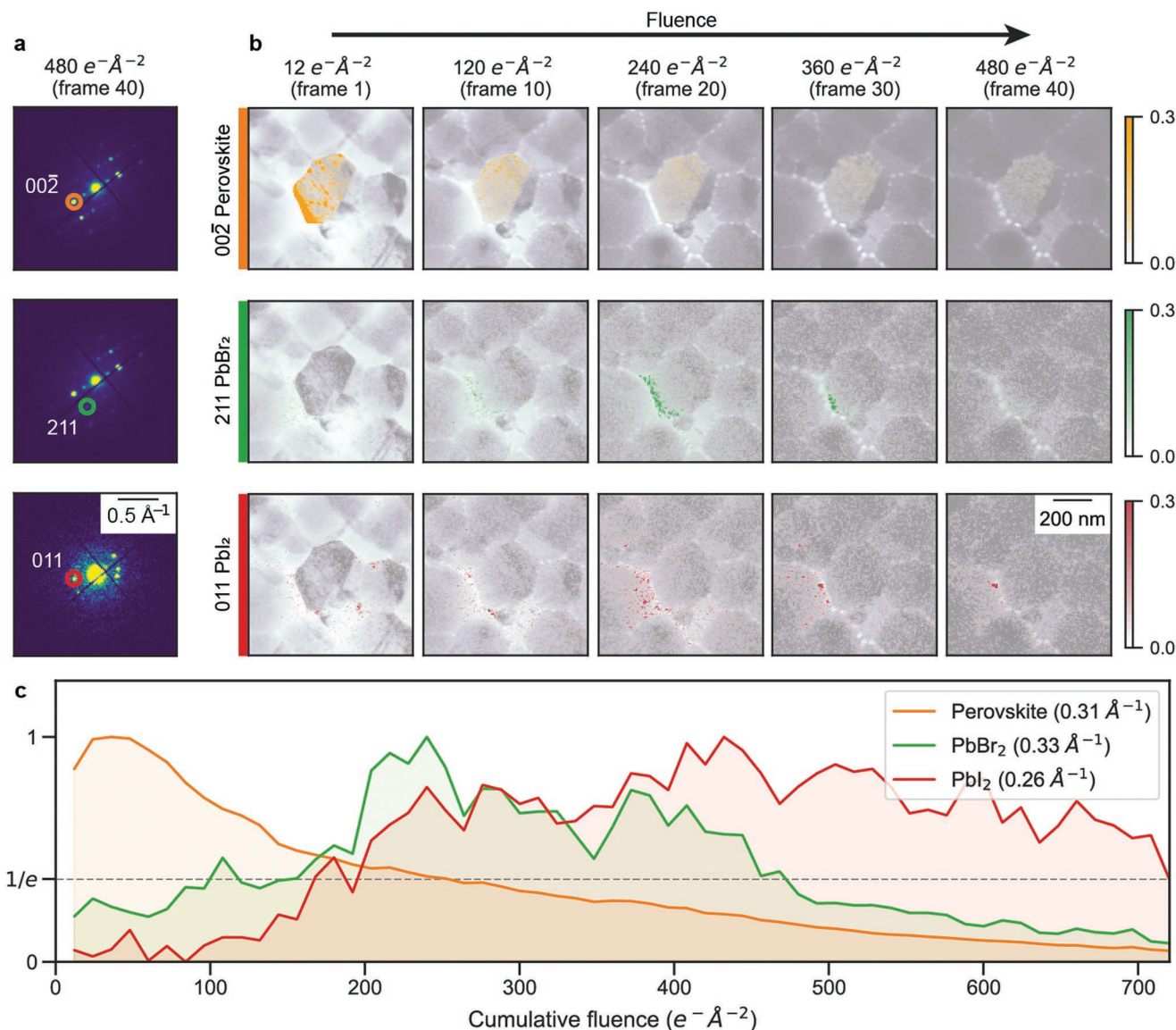


**Figure 3.** Mapping the evolution of the degradation species in a  $(\text{FA}_{0.79}\text{MA}_{0.16}\text{Cs}_{0.05})\text{Pb}(\text{I}_{0.83}\text{Br}_{0.17})_3$  film. a) The diffraction patterns at the 40th frame, taken from region 1 in Figure 2 for the perovskite and  $\text{PbBr}_2$  series, and from region 2 in Figure 2 for  $\text{PbI}_2$ . For each diffraction pattern, a dark-field virtual aperture is selected. b) vDF images of the respective virtual apertures placed at: the (002) perovskite reflection (orange), the (211)  $\text{PbBr}_2$  reflection observed within the grains (green), and the (011)  $\text{PbI}_2$  reflection localized at the high-angle grain boundary (red). The color scale range is set to 30% to better show the small changes in intensity. All vDF images are superimposed on top of the respective vBF images. c) Intensity profiles taken from the perovskite (002), the  $\text{PbBr}_2$  (211), and the  $\text{PbI}_2$  (011) reflections. The  $1/e$  intensity threshold is shown with a dashed line.

has reached  $\approx 1/e$  relative to its initial value, is  $\approx 200 e^{-\text{\AA}^{-2}}$ . At this critical fluence, the lead halide phases start to emerge. The critical fluence reported here is in close agreement with those by Rothmann et al. for the pure  $\text{FAPbI}_3$  composition.<sup>[23]</sup> We investigated other grains from adjacent regions, all of which exhibited similar progressive grain amorphization with an equivalent critical fluence (see Figure S14, Supporting Information).

The nature of the grain boundaries affects the degradation pathway. High-angle grain boundaries, labeled as 1 and 2 in Figure 4, are associated with the nucleation and growth of pinholes. Not all grain boundaries exhibit pinhole formation to the same extent, exemplified by region 2 being more altered than region 1 (Figure 4a). The initial diffraction pattern at this region

reveals region 2 to show not only reflections attributed to the perovskite adjacent grains, but also additional reflections and diffuse scattering. Although these additional reflections, already visible in the first frame, are difficult to index, they suggest the presence of defects.<sup>[46]</sup> These defective high-angle boundaries can trigger faster degradation and larger morphological variations than less defective boundaries (region 1).

In the schematic in Figure 4d, we propose a degradation mechanism whereby iodine segregation toward the grain boundary leaves bromine-rich areas within the perovskite grains, which form  $\text{PbBr}_2$  at the surface to balance the iodine deficiency. Both  $\text{PbI}_2$  and  $\text{PbBr}_2$  are more thermodynamically stable and have higher thermal conductivity than the parent

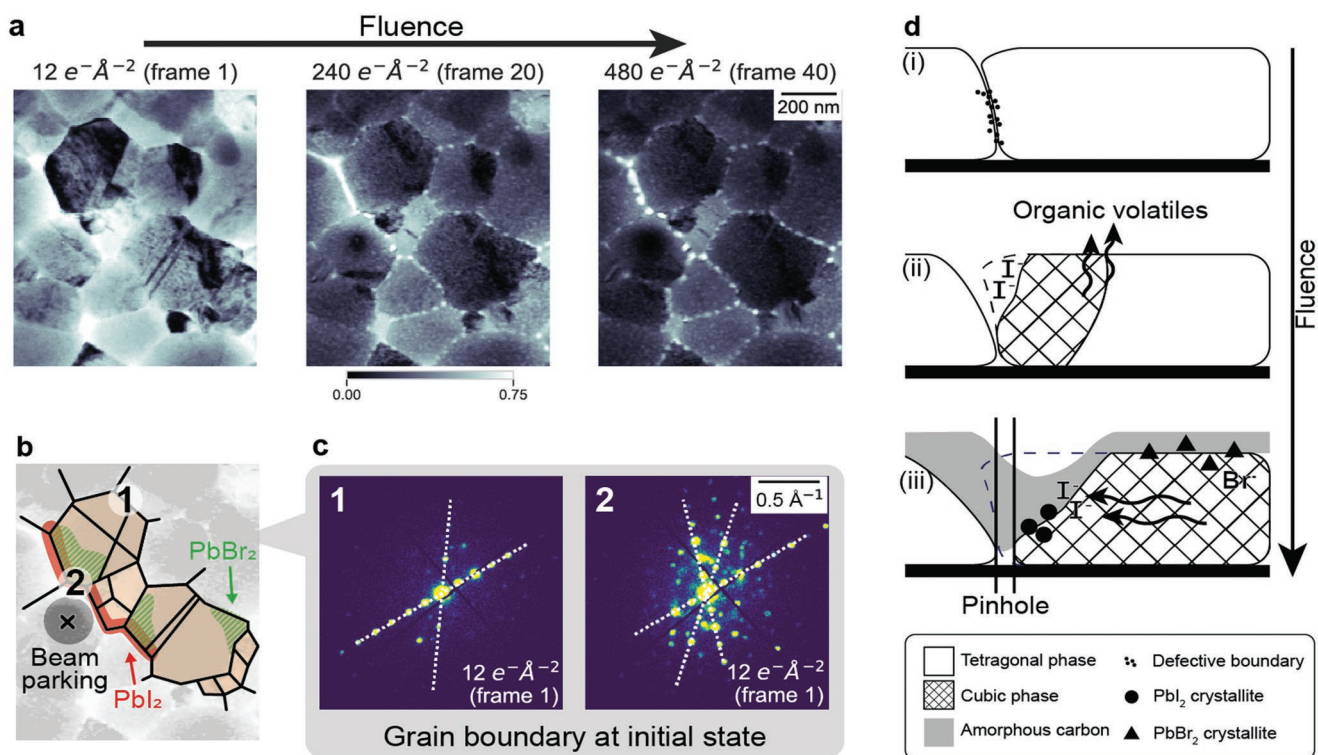


**Figure 4.** The grain boundaries in a  $(\text{FA}_{0.79}\text{MA}_{0.16}\text{Cs}_{0.05})\text{Pb}(\text{I}_{0.83}\text{Br}_{0.17})_3$  film affect the degradation pathway. a) Evolution of vBF images of various grains and surrounding grains after up to  $480 \text{ e}^- \text{Å}^{-2}$  fluence, showing stark changes in the morphology. b) Schematic of multiple perovskite grains from which  $\text{PbI}_2$  and  $\text{PbBr}_2$  species are observed. The regions from which diffraction patterns are extracted are labeled as 1 and 2. c) Diffraction patterns for two high-angle grain boundaries: in region 1 a grain boundary exhibiting the reflections only attributed to the perovskite phase of the grains at either side of the boundary, and in region 2 a grain boundary also exhibiting additional reflections and diffuse scattering, typical of amorphous defective phases. d) Schematic of the degradation mechanisms and factors identified during degradation at high fluences, in cross-section view.

hybrid perovskite. The transformation dissipates energy and heat more effectively. These processes happen in conjunction with the loss of the more volatile  $\text{I}_2$  and organic moieties. These changes result in a tetragonal to cubic phase transition, the formation of small  $\text{PbI}_2$  crystallites at the grain boundaries with pinholes, and the redeposition of some organics as a thin amorphous organic film on the surface of the specimen.

A grain near the  $[001]$  zone axis, which exhibits superlattice reflections attributed to the  $\text{BX}_6$  corner-sharing octahedra tilted away from perfect cubic symmetry toward the tetragonal perovskite phase,<sup>[38]</sup> shows a progressive loss of these superstructure reflections (see Figure S15, Supporting Information). These changes upon electron exposure suggest a gradual transformation from tetragonal to cubic structure, expected with the loss of the organic cations and in agreement with the proposed degradation mechanism.

In this SED experiment, the beam parking position was set at the center of the image frame, as shown in Figure 3b, causing overexposure within the field of view. This may cause additional damage to the grain under beam parking and its boundaries, and trigger faster degradation. However, similar degradation pathways are observed in grains that are not adjacent to the beam parking position. For example, we see additional  $\text{PbBr}_2$  reflections emerging after a fluence of  $\approx 252 \text{ e}^- \text{Å}^{-2}$  from another grain oriented near  $[100]$  (Figures S12 and S13, Supporting Information).

Finally, we perform analogous scanning probe synchrotron nXRD measurements to acquire a similar 5D dataset by combining a time series stack of multiple nXRD frames. Such acquisition allows us to study the interaction of highly converged 20 keV X-rays on nominally equivalent triple cation composition perovskite films as previously presented for electrons. The use of nXRD allows for close comparison with SED because it similarly involves scanning over a localized region of interest. Unlike SED, this technique cannot access subgrain features under these conditions, as the X-ray beam diameter is  $\approx 150 \text{ nm}$ . Figure 5a shows the spatially averaged 1D diffraction patterns across a scanned area of  $\approx 4 \mu\text{m}^2$  for X-ray photon fluences up to  $7750 \text{ photons Å}^{-2}$ .

The main diffraction peaks are indexed to the same tetragonal  $P4/mbm$  perovskite phase as in SED. Some crystallographic plane reflections are more prevalent and decay more slowly, which can be linked to the crystal structure.  $(110)$ ,  $(220)$ ,  $(130)$ , and  $(222)$  planes are the brightest reflections. The diffraction intensity at these planes is strongly affected by the loss of the halogen atoms from the unit cell since these planes cut mainly across halide positions (see the simulation in Figure S16, Supporting Information). In contrast,  $(111)$ ,  $(021)$ , and  $(131)$  planes diffract less strongly, and their relative intensity is more affected by the loss of the organic cations since all contain A+X ion sublattices. In fact, the  $(220)$  and  $(130)$  planes exhibit the slowest decay rate (see Figure S16, Supporting Information),

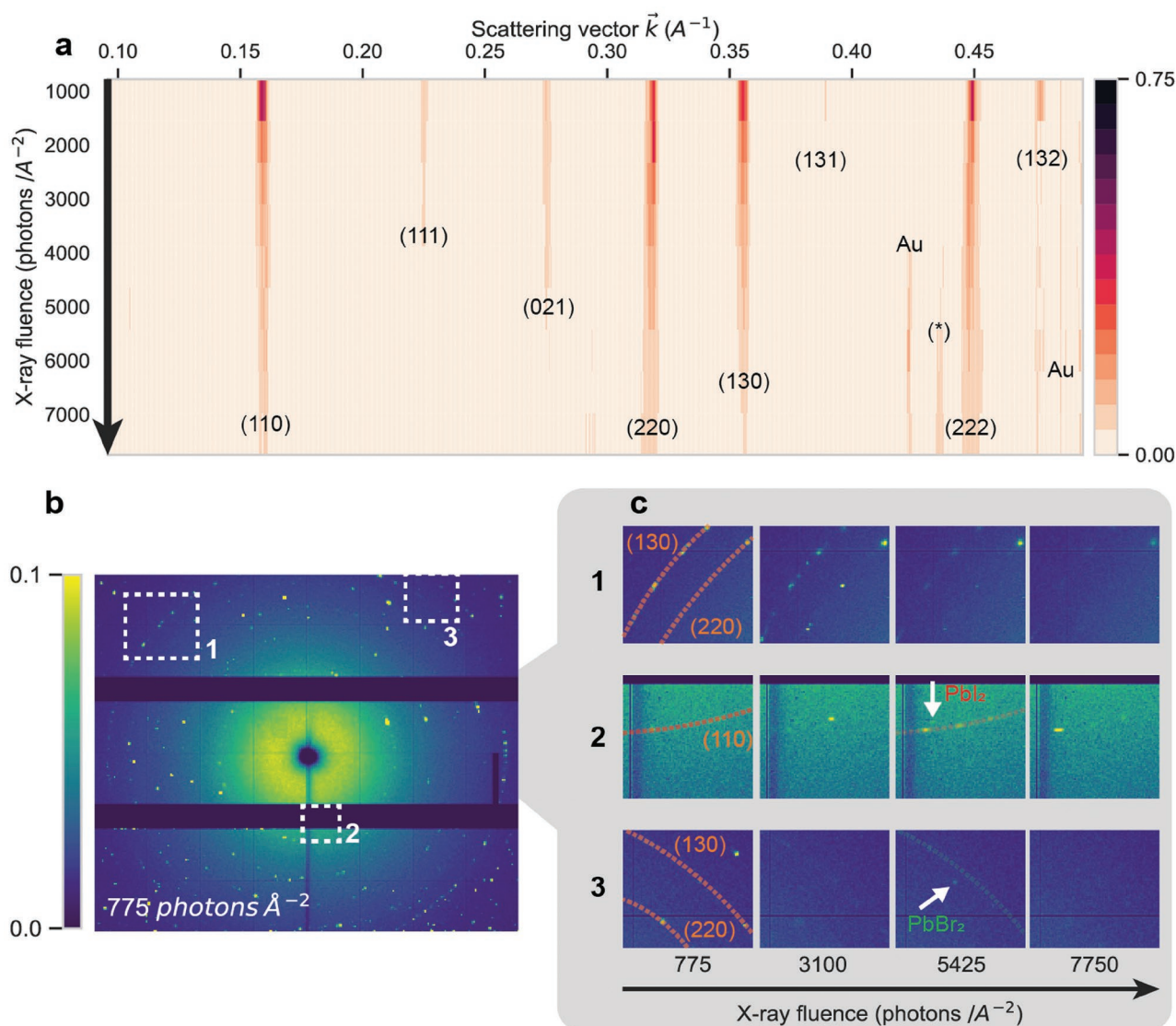


**Figure 5.** Probing the evolution of the local structure of a region in a  $(\text{FA}_{0.79}\text{MA}_{0.15}\text{Cs}_{0.06})\text{Pb}(\text{I}_{0.85}\text{Br}_{0.15})_3$  halide perovskite film under X-ray exposure using nXRD. a) Radially integrated nXRD evolution of a perovskite film over accumulated illumination over an area of  $4 \mu\text{m}^2$ . Peaks are indexed to the  $P4/mbm$  perovskite phase. The peak marked as (\*) cannot be indexed to perovskite and corresponds mainly to the degradation phases. To analyze the weak reflections lost during radial integration, 2D nXRD diffraction patterns are shown in (b), with some areas of interest denoted by numerals. c) The zoomed-in evolution of nXRD in 2D elucidates crystal tilting in region 1, the weak appearance of (002) 4H- $\text{PbI}_2$  in region 2, and the appearance of (211)  $\text{PbBr}_2$  reflections in region 3. These findings are similar to the changes observed in SED.

suggesting the rapid loss of the organic cation followed by the slower loss of the halides. The loss of I and Br can be further analyzed from the nXRF, acquired simultaneously to the nXRD data, in which the  $\text{I}_{\text{La}}$  signal systematically drops before the  $\text{Br}_{\text{Ka}}$  signal (see Figure S17, Supporting Information), suggesting  $\text{I}_2$  to be more volatile than  $\text{Br}_2$ .<sup>[47]</sup>

The (110), (220), and (130) plane reflections brighten after two to four frames ( $\approx 1400$ – $2800 \text{ photons } \text{\AA}^{-2}$ ). A closer examination of these reflections in the 2D patterns (Figure 5c, region 1) reveals the appearance of additional Bragg reflections of the crystal planes, attributed to the crystals tilting closer to the zone axis, similar to the SED findings in Figure 1 albeit in nXRD we are sampling multiple grains.

Some weak and broad reflections appear after five frames ( $4650 \text{ photons } \text{\AA}^{-2}$ ) in the range  $\approx 0.436 \pm 0.003 \text{ \AA}^{-1}$  (Figure 5a, marked with \*). These reflections are not indexable to the perovskite structure and can be used to arbitrarily determine the X-ray critical exposure of hybrid perovskite systems. This critical exposure value is one order of magnitude higher than previously reported values for  $\text{MAPbBr}_3$  single crystals ( $10^2 \text{ photons } \text{\AA}^{-2}$ ), at which point the scattering image had changed by more than 10%, but it is lower than for  $\text{CsPbBr}_3$  single crystals ( $10^4 \text{ photons } \text{\AA}^{-2}$ ).<sup>[25]</sup> We also performed the same synchrotron diffraction degradation experiments using a static 17.2 keV X-ray box-beam with a wider illumination area of  $\approx 1 \mu\text{m}^2$  (see Figure S18, Supporting Information). The nonlocalized

nature of the exposure required two to three orders of magnitude higher fluence ( $\approx 5 \times 10^6$  photons  $\text{\AA}^{-2}$ ) to acquire similar diffraction information and produce a similar degradation pattern as for nXRD.

The reflection at  $\approx 0.436 \pm 0.003 \text{\AA}^{-1}$  matches the (110) 4H-PbI<sub>2</sub> plane, but also matches phases like PbBr<sub>2</sub> or polyphases. A closer examination of the 2D diffraction patterns reveals extremely weak additional reflections appearing, indexable to both (002) 4H-PbI<sub>2</sub> and (211) PbBr<sub>2</sub> (Figure 5c region 2 and 3, respectively). As these reflections are lost during radial integration, it is critical to analyze the full 2D data sets (see more examples in Figure S19, Supporting Information).

Our combined results offer an understanding of the changes induced by the interaction of electrons and X-rays with hybrid halide perovskite semiconductors. Each diffraction technique used offers some advantages over the other. nXRD provides excellent resolution in reciprocal space, but lower resolution in real space. X-ray-based techniques are extremely useful to discern crystal structures with similar features. Since many of the degradation changes occur on the nanoscale, nXRD in general is unable to spatially resolve such changes.

In contrast, SED offers excellent spatial resolution and allows mapping of crystallographic changes at the nanometer scale. However, in SED, points in reciprocal space are broadened by a shape factor and spread out forming disks, due to the use of thin samples and a finite convergence semiangle, respectively. Multiple of these diffraction disks are intersected by the lower curvature of the Ewald sphere, compared to X-rays, limiting the resolution in reciprocal space of SED. Due to the similarity between pristine and intermediate perovskite degradation phases such as the 2H, 4H, and 6H polytypes,<sup>[28]</sup> SED is not able to unambiguously assign similar structures. Moreover, due to the constrained acquisition geometry, not all grains produce interpretable SED patterns near a low-order zone axis. Further studies using precession electron diffraction, which offers more complete integration of the diffraction space, could overcome the latter constraint if performed under low fluences.<sup>[48]</sup>

The different nature of electrons and photons results in distinctive interactions with the specimen. For example, when electrons propagate through a material, they undergo elastic Bragg scattering and inelastic scattering. For a 200 kV beam, each inelastically scattered electron transfers  $\approx 27$  eV per scattering event to the specimen (see Table S1, Supporting Information). This results in knock-on damage, radiolytic damage, and local heating.<sup>[13]</sup> For a 200 nm thick film of the perovskite composition studied here at 200 keV, we estimate the probability of inelastic scattering to be twice that of no inelastic scattering (calculated with the Poisson model in the Supporting Information).<sup>[49]</sup> The ratio of elastic versus inelastic cross-sections is inversely proportional to atomic number (proportional to  $19 \cdot Z^{-1}$  for electrons of hundreds of keV).<sup>[49]</sup> For the triple cation perovskite composition, similar elastic and inelastic scattering probabilities are expected, based on the effective atomic number ( $Z = 36.4$ ). However, carbon atoms will contribute more to, and be more affected by, inelastic scattering than iodine or bromine, by a factor of 8 and 6, respectively. This is consistent with the damage mechanism proposed, in which the organic cations are the weaker species, and the halides restructure chemically to more stable intermediates. The effect of the

inelastic cross-sections can be reduced by using thinner specimens or higher acceleration voltages, both of which will reduce the accessible diffraction information. A fine balance between these parameters is key. For the X-ray photons of tens of keV, the perovskite film is virtually transparent (see calculations in the Supporting Information). However, inelastic scattering is also always present in XRD, with a ratio of inelastic to elastic scattering cross-sections also inversely proportional to atomic number by  $50 \cdot Z^{-1.7}$  for 20 keV photons. These ratios highlight the higher need to account for photon beam damage when X-rays are used on hybrid materials, especially for prolonged exposures (see estimations in the Supporting Information and Figure S20, Supporting Information).

Similar mechanisms of interaction and damage can be seen with both electron and X-ray probes. Grains tend to tilt by a few degrees toward the zone axis after the first frames of acquisition ( $\approx 100 \text{ e}^- \text{\AA}^{-2}$  and  $\approx 1400\text{--}2800$  photons  $\text{\AA}^{-2}$ ). We attribute these changes to nondestructive changes at the nanoscale, yet beam-assisted annealing of the prestrained films on the SiN support membrane cannot be excluded. These findings are important as they place constraints on the use of such techniques for elucidating the pristine microstructure of halide perovskites. Radiation exposure also leads to loss of crystallinity in the grains and degradation of the perovskite structure, with a critical fluence of  $<200 \text{ e}^- \text{\AA}^{-2}$  and  $<5000$  photons  $\text{\AA}^{-2}$  for SED and nXRD, respectively. The degradation mechanism proposed in this work is in agreement with the high-resolution-STEM work on FAPbI<sub>3</sub> evaporated films by Rothmann et al., in which PbI<sub>2</sub> precipitates epitaxially grow from the perovskite.<sup>[23]</sup> However, we observe crucial differences given by the more complex perovskite composition used in this study, in which simultaneous formation of PbBr<sub>2</sub> is also observed at the grains, potentially aided by the higher volatility of I<sub>2</sub> compared to Br<sub>2</sub>, by the higher surface area present at the grain boundaries, and by small nanoscale chemical heterogeneity at the grain boundaries.<sup>[42,43]</sup> These findings can be extended to the radiation damage from a high-energy X-ray nanobeam, which also results in the emergence of lead halide species upon loss of the organic moieties across the whole scanned area (Figure S17, Supporting Information). In fact, the presence of the organic cation species at the A position has been proposed to trigger degradation processes toward PbI<sub>2</sub> as opposed to the Pb<sup>0</sup>, mostly only seen from inorganic compositions, as the organics can undergo radiolysis more easily than the Pb<sup>2+</sup> cation upon electron and X-ray illumination.<sup>[22,50]</sup> Future work should focus on combining the microscopy techniques used here with the passivation strategies that have been successfully employed in halide perovskite semiconductors (passivation by coordinate bonding, ionic bonding, or chemical conversion),<sup>[51]</sup> to gain better understanding of the chemistry of passivation in hybrid halide perovskites. In fact, SED was recently used to understand the effect of surface-bound passivation agents on the crystallinity of halide perovskites by means of octahedral tilting stabilization.<sup>[38]</sup>

The degradation mechanism proposed here contrasts with the degradation pathways observed from light-soaking. Photo-carriers produced during light soaking can trigger the formation of I<sub>2</sub> via redox-mediated reactions, leaving metallic Pb<sup>0</sup> and pinholes behind. Such changes are proposed to be seeded from crystallographic and compositional impurities.<sup>[46]</sup> Light soaking

can also trigger Cs segregation,<sup>[52]</sup> which is not observed in the nXRF mapping during high-energy X-ray exposure in this report (see Figure S17, Supporting Information). The use of high-energy beams results in faster degradation pathways of perovskites from the pristine state, compared to early-stage degradation from impurities caused by lower-fluence visible light irradiation. We note that large charge carrier densities are estimated to be created during acquisition, ranging around  $10^{16}$  to  $10^{19}$   $e^-h^+$ -pairs  $cm^{-3}$  for SED, and  $10^{19}$   $e^-h^+$ -pairs  $cm^{-3}$  for nXRD (see estimations in the Supporting Information). Such large localized hot carriers can trigger radicals, multiparticle recombination, and thermalization processes on top of the knock-on damage, radiolytic damage, and local heating caused by the high-energy particle beam. Therefore, such high carrier concentrations can promote degradation of the perovskite in ways distinct from those encountered under illumination at 1 sun ( $10^{14}$  to  $10^{16}$  carriers  $cm^{-3}$ , mostly generated at band edge), likely aiding in the radiolysis of the organic cations in the perovskite.<sup>[50]</sup>

The radiation hardness described here suggests good resilience of these materials to degradation from electron radiation in space. Assuming radiation damage of hybrid perovskite being dependent on the total dose rather than on the dose rate,<sup>[11,12]</sup> the critical fluence for electrons would be accumulated after around  $\approx 2000$  years in the Earth orbit or  $\approx 200$  years at harsher orbits like Jupiter (see Figure S21, Supporting Information). We note the differences between electron radiation in microscopes and space, such as the energy spectrum of space radiation extending up to 1 MeV energies, and the generally lower radiation fluxes in orbit.<sup>[6,9]</sup> Combined with the reported excellent proton radiation hardness,<sup>[6,8]</sup> this study once more places halide perovskites as promising candidates for space photovoltaic applications. Further studies should also include the effect of cryogenic temperatures on the degradation of halide perovskites.

### 3. Conclusion

Our conclusions have implications for understanding the changes on the nanoscale of halide perovskites upon interaction with high-energy radiation, in particular electrons and X-rays. We have identified local changes on the nanostructure at extremely low radiation exposure, leading to changes in the orientation of the grains. At high radiation exposure, degradation of the perovskite phase involves iodine migration, producing decomposition to lead halide species.  $PbBr_2$  reflections appear within perovskite grains that exhibit  $PbI_2$  crystallites growing at their grain boundaries. Specifically, regions showing high-angle defective grain boundaries are important for degradation. Passivation and growth strategies targeting the removal of such high-angle defective grain boundaries will be critical for the further mitigation of halide perovskite instabilities, especially for applications vulnerable to high-energy radiation. By combining known passivation strategies with novel microscopy techniques such as those described here, a better understanding of the chemistry of passivation in hybrid halide perovskites can be acquired and help move its applications forward. Finally, the findings reported here provide a further understanding of the

exposure limits of high-energy electron and photon beams, being  $<200 e^- \text{Å}^{-2}$  at 200 keV and  $<5000$  photons  $\text{Å}^{-2}$  at 20 keV, respectively. These critical radiation exposure methodologies are crucial for any characterization technique used to study the nanoscale of halide perovskites and, more generally, can be extended to any soft semiconductor, as well as to further understand the challenges that perovskite solar cells still face for space applications.

### 4. Experimental Section

**Sample Preparation:** All procedures were followed inside an inert  $N_2$ -gas glovebox. The perovskite precursors solutions were prepared by first dissolving FAI (1.0 M) and MABr (0.2 M),  $PbI_2$  (1.1 M), and  $PbBr_2$  (0.22 M) in a mixture of anhydrous dimethylformamide (DMF) and dimethyl sulfoxide (DMSO) (4:1 v:v). A solution of CsI (1.5 M in DMSO) was then added to the precursor solution as 5% of the total volume, yielding a nominal  $(FA_{0.79}MA_{0.16}Cs_{0.05})Pb(I_{0.83}Br_{0.17})_3$  perovskite precursor composition. Lead halide precursors were supplied by TCI, organic compounds were supplied by Greatcell Solar, and CsI and solvents were supplied by Sigma.

To fabricate thin electron-transparent specimens for SED, the perovskite solution was diluted in anhydrous DMF:DMSO 4:1 v:v in a 2:1 ratio of diluent to precursor solution, and spin-coated on SiN TEM grids with a 30 nm thick low-stress amorphous  $Si_3N_4$  membrane window (NT025X, Norcada). Spin-coating was followed in two steps at 2000 and 6000 rpm for 10 and 35 s, respectively, with 20  $\mu$ L of chlorobenzene added 30 s before the end of the second step. The films were then annealed at 100 °C for 1 h, yielding films of  $\approx 200$  nm.

To fabricate thin films for the nXRD studies, the same protocol was used to prepare an almost nominally identical perovskite precursor solution of  $(FA_{0.79}MA_{0.15}Cs_{0.06})Pb(I_{0.85}Br_{0.15})_3$ . The precursor was then spin-coated on X-ray transparent windows (Norcada, NX7100C), following the same protocol as for the SED samples, and then annealed, yielding films of  $\approx 500$ – $600$  nm.

**SED:** During SED microscopy, a 2D electron diffraction pattern was measured at every probe position of an electron beam in STEM mode. SED data were acquired on the JEOL ARM300CF E02 instrument at ePSIC (Diamond Light Source, Didcot-Oxford, UK). A monolithic Merlin/Medipix direct electron detector with 4 back-contacts was used to acquire fast low-dose SED. These direct electron detectors allow for better SNR under lower doses due to the superior quantum efficiency compared to traditional CCD. The detector was set to 6-bit, to maintain the targeted electron fluence and fast acquisition readout rate. In the initial frames of the acquisition, some diffraction patterns exhibited saturation at the direct beam position, due to the bit-depth limitations of the direct electron detector imposed by the fast low-dose acquisition conditions. Such saturated pixels are occasional but visible as the brightest pixels in Figure 1b. The beam blanking after each frame was performed manually, always at the same controlled localized position and after a reaction time of  $\approx 500$  ms. An acceleration voltage of 200 keV, nanobeam alignment (convergence semiangle  $\approx 1$  mrad), electron probe  $\approx 5$  nm, probe current  $\approx 3.59$  pA, scan dwell time 1 ms, and camera length 20 cm. Post-processing of SED diffraction data was done using pyXem 0.12 (an open-source Python library based on HyperSpy-based for crystallographic electron microscopy).<sup>[53]</sup>

Virtual bright-field images (vBF) were referred as the images reconstructed from taking the intensity integrated solely from the direct beam as a function of probe position, thus only containing information from the electrons recorded at zero scattering angle. Contrarily, virtual dark-field images (vDF) were reconstructed from only taking the intensity from a Bragg-diffracted spot from the 2D diffraction pattern as a function of probe position, thus containing information solely on electrons scattered to specific Bragg angles. All virtual apertures for vBF

mapping were set to  $4 \times 10^{-3} \text{ \AA}^{-1}$  (2.4 mrad of semiangle of detector), and for vDF were set to  $2\text{--}4 \times 10^{-3} \text{ \AA}^{-1}$  at diffraction semiangles ranging between 0 and 70 mrad.

All diffraction patterns were distortion corrected and calibrated with an Au cross grating. The drift in the beam position of the nonscattered beam was corrected and centered for all frames using cross-correlation with a subpixel factor of 10. To display diffraction planes that match real-space features, all diffraction patterns shown in the main text were rotation corrected using a MoO<sub>3</sub> calibration sample. Dead pixels and detector junctions were masked. No sample drift correction was necessary. Finally, the background noise in all diffraction patterns was filtered, setting a threshold of detector pixels with single counts to zero.

**nXRD:** Scanning nano-XRD data were acquired at the synchrotron beamline I14 of the Diamond Light Source (Didcot-Oxford, UK). 2D diffraction patterns were recorded at each stage position as the specimen was moved through the X-ray beam. An array of 3 Medipix 2048 × 512 pixel arrays in transmission mode (Excalibur 3M) was used to acquire diffraction data. To examine the effect of repeated maps on the same region of a film, a scan loop was measured within a  $5 \times 5 \text{ \mu m}$  region until most of the diffraction spots were no longer visible. A 20 keV monochromatic X-ray beam ( $\lambda = 0.619 \text{ nm}$ ) was used, focused to  $\approx 150 \text{ nm}$ . Samples were mounted onto the I14 standard sample holder and measured under a local flow of dry N<sub>2</sub> to suppress perovskite degradation that was accelerated by moisture and oxygen. 2D sum patterns across the scanned region were used without processing. 1D patterns were radially integrated using the Data Analysis Workbench (DAWN) with a CeO<sub>2</sub> calibration standard and a mask to remove dead pixels and detector edges.<sup>[54]</sup> The 1D sum pattern for each frame was cropped from  $0.6 \text{ \AA}^{-1}$  onward and Origin Pro was used to subtract a baseline found from 20 baseline anchor points found via the 2nd derivatives and connected by line interpolation. Simultaneous X-ray fluorescence (nXRF) data were acquired with a 4 element Si drift detector. The nXRF maps were aligned using the Au<sub>Lα</sub> peaks and the summed signals across the scanned area were found for Pb<sub>Lα</sub>, I<sub>Lα</sub>, and Br<sub>Kα</sub>.

All diffraction patterns in this work were reported in “ordinary” wavevectors ( $k = 1/d$ ). Note that these units differed from the “angular” wavevectors definition ( $q = 2\pi/d$ ) by a factor of  $2\pi$ , which is often used in X-ray crystallography literature.

**Crystal Structure Library:** All diffraction patterns from this work could be closely indexed to a pseudo-cubic/tetragonal perovskite unit cell (*P4/mbm*) with lattice parameters of  $a = b = 9.00$  and  $c = 6.36 \text{ \AA}$ . Despite the stoichiometry of the sample being the complex (FA<sub>0.79</sub>MA<sub>0.16</sub>CS<sub>0.05</sub>)Pb(I<sub>0.83</sub>Br<sub>0.17</sub>)<sub>3</sub> perovskite composition, it could be approximated as a simpler unit cell made from the predominant ion at each site (C, Pb and I) and with manually scaled lattice parameters to fit the experimental observations. Any variations that would occur in diffraction patterns between the simpler model used here and the more complex structure were minor and hard to discern in the reciprocal-space resolution of SED technique (under acquisition conditions one pixel in the detector was  $0.0046 \text{ \AA}^{-1}$ ).

A series of different plausible degradation crystal structures were also considered, to attempt the indexing of some of the additional reflections appearing after radiation exposure. In general, the hexagonal 4H-PbI<sub>2</sub> crystal phase (*P63mc*, lattice parameters of  $a = b = 4.56$  and  $c = 13.96 \text{ \AA}$ , COD ID: 9009140) and the orthorhombic PbBr<sub>2</sub> crystal phase (*Pnam*, COD ID: 1530324, lattice parameters of  $a = 80.6$ ,  $b = 6.54$  and  $c = 4.73 \text{ \AA}$ ) were found to match the diffraction patterns discussed in this work. The structure files were retrieved from the crystallography open database.<sup>[55,56]</sup> However, other plausible degradation phases were also considered but did not match experimental data, such as perovskite intermediate polytypes, which are more extensively described in the Supporting Information, or the other 2H- and 6H-PbI<sub>2</sub> polytypes reported by others as a degradation product.<sup>[20,23]</sup> However, despite some ambiguity on the specific PbI<sub>2</sub> polytype across literature, since these phases were remarkably similar,<sup>[41]</sup> the formation of small precipitates of PbI<sub>2</sub> was observed.

All diffraction simulations were performed using Single Crystal 4 (CrystalMaker Software Limited), adjusting the simulation parameters to resemble the experimental data (200 keV, detector spot size  $0.025 \text{ \AA}^{-1}$ , saturation 10, gamma 2). Simulation files in “.scdx” format can be found in the Supporting Data.

## Supporting Information

Supporting Information is available from the Wiley Online Library or from the author.

## Acknowledgements

J.F.O. and C.D. acknowledge funding from the Engineering and Physical Sciences Research Council (EPSRC) Nano Doctoral Training Centre (EP/L015978/1). T.A.S.D. acknowledges funding from a National University of Ireland Travelling Studentship. J.F.O., T.A.S.D., and S.D.S. acknowledge the European Research Council (ERC) under the European Union’s Horizon 2020 research and innovation programme (HYPERION, grant agreement no. 756962). S.D.S. acknowledges support from the Royal Society and Tata Group (UF150033). The authors acknowledge funding from the EPSRC (EP/R023980/1, EP/W004445/1) and from the EPSRC Centre for Advanced Materials for Integrated Energy Systems (CAM-IES, EP/P007767/1). SED studies were supported by the access to e02 at ePSIC (MG25250) and nXRD studies were supported by access to the I14 beamline (SP-20420). Mohsen Danaie and Julia Parker are acknowledged for their support during the acquisition and calibration of the SED and nXRD data, respectively.

## Conflict of Interest

S.D.S. is a co-founder of Swift Solar, Inc.

## Author Contributions

J.F.O. analyzed and interpreted SED, nXRD, and sXRD data. T.A.S.D. prepared samples and acquired the microscopy datasets and assisted with the interpretation of the data. D.N.J. and S.M.C. aided in the acquisition and interpretation of SED data. P.A.M. supervised D.N.J. and aided in the interpretation of SED data. H.S. assisted in the data acquisition of data. S.D.S. supervised J.F.O. and T.A.S.D. and provided input on data interpretations. C.D. supervised J.F.O. and provided input on data interpretations. J.F.O. wrote the manuscript with input from all authors.

## Data Availability Statement

The data that support the findings of this study are openly available in Apollo, the University of Cambridge Repository, at <https://doi.org/10.17863/CAM.82486>.

## Keywords

high-energy beam damage, lead halide perovskites, nano-X-ray diffraction, nanoprobe diffraction, scanning electron diffraction

Received: January 13, 2022

Revised: February 28, 2022

Published online:

- [1] E. M. Tennyson, T. A. S. Doherty, S. D. Stranks, *Nat. Rev. Mater.* **2019**, *4*, 573.
- [2] C. A. R. Perini, T. A. S. Doherty, S. D. Stranks, J.-P. Correa-Baena, R. L. Z. Hoyer, *Joule* **2021**, *5*, 1024.
- [3] J. F. Galisteo-López, M. E. Calvo, H. Míguez, *Adv. Opt. Mater.* **2021**, *9*, 2100133.
- [4] A. S. Eggeman, *Acta Crystallogr., Sect. B: Struct. Sci., Cryst. Eng. Mater.* **2019**, *75*, 475.
- [5] M. Kodur, R. E. Kumar, Y. Luo, D. N. Cakan, X. Li, M. Stuckelberger, D. P. Fenning, *Adv. Energy Mater.* **2020**, *10*, 1903170.
- [6] Y. Tu, J. Wu, G. Xu, X. Yang, R. Cai, Q. Gong, R. Zhu, W. Huang, *Adv. Mater.* **2021**, *33*, 2006545.
- [7] Y. Murakami, F. Ishiwari, K. Okamoto, T. Kozawa, A. Saeki, *ACS Appl. Mater. Interfaces* **2021**, *13*, 24824.
- [8] F. Lang, M. Jošt, J. Bundesmann, A. Denker, S. Albrecht, G. Landi, H.-C. Neitzert, J. Rappich, N. H. Nickel, *Energy Environ. Sci.* **2019**, *12*, 1634.
- [9] T. Markvart, *J. Mater. Sci.: Mater. Electron.* **1990**, *1*, 1.
- [10] S. É. Bourdarie, M. Xapsos, *IEEE Trans. Nucl. Sci.* **2008**, *55*, 1810.
- [11] M. U. Rothmann, W. Li, Y. Zhu, A. Liu, Z. Ku, U. Bach, J. Etheridge, Y. B. Cheng, *Adv. Mater.* **2018**, *30*, 1800629.
- [12] J. Ran, O. O. Dyck, X. Wang, B. Yang, D. B. Geohegan, K. Xiao, *Adv. Energy Mater.* **2020**, *10*, 1903191.
- [13] S. Chen, P. Gao, *J. Appl. Phys.* **2020**, *128*, 010901.
- [14] S. Chen, Y. Zhang, J. Zhao, Z. Mi, J. Zhang, J. Cao, J. Feng, G. Zhang, J. Qi, J. Li, P. Gao, *Sci. Bull.* **2020**, *65*, 1643.
- [15] S. Chen, X. Zhang, J. Zhao, Y. Zhang, G. Kong, Q. Li, N. Li, Y. Yu, N. Xu, J. Zhang, K. Liu, Q. Zhao, J. Cao, J. Feng, X. Li, J. Qi, D. Yu, J. Li, P. Gao, *Nat. Commun.* **2018**, *9*, 4807.
- [16] S. Chen, C. Wu, B. Han, Z. Liu, Z. Mi, W. Hao, J. Zhao, X. Wang, Q. Zhang, K. Liu, J. Qi, J. Cao, J. Feng, D. Yu, J. Li, P. Gao, *Nat. Commun.* **2021**, *12*, 5516.
- [17] C. Xiao, Z. Li, H. Guthrey, J. Moseley, Y. Yang, S. Wozny, H. Moutinho, B. To, J. J. Berry, B. Gorman, Y. Yan, K. Zhu, M. Al-Jassim, *J. Phys. Chem. C* **2015**, *119*, 26904.
- [18] N. Klein-Kedem, D. Cahen, G. Hodes, *Acc. Chem. Res.* **2016**, *49*, 347.
- [19] A. R. Milosavljević, W. Huang, S. Sadhu, S. Ptasińska, *Angew. Chem., Int. Ed.* **2016**, *55*, 10083.
- [20] A. Alberti, C. Bongiorno, E. Smecca, I. Deretzis, A. La Magna, C. Spinella, *Nat. Commun.* **2019**, *10*, 2196.
- [21] Z. Dang, J. Shamsi, F. Palazon, M. Imran, Q. A. Akkerman, S. Park, G. Bertoni, M. Prato, R. Brescia, L. Manna, *ACS Nano* **2017**, *11*, 2124.
- [22] X.-G. Zhou, C.-Q. Yang, X. Sang, W. Li, L. Wang, Z.-W. Yin, J.-R. Han, Y. Li, X. Ke, Z.-Y. Hu, Y.-B. Cheng, G. Van Tendeloo, *J. Phys. Chem. C* **2021**, *125*, 10786.
- [23] M. U. Rothmann, J. S. Kim, J. Borchert, K. B. Lohmann, C. M. O'Leary, A. A. Shearer, L. Clark, H. J. Snaith, M. B. Johnston, P. D. Nellist, L. M. Herz, *Science* **2020**, *370*, eabb5940.
- [24] M. Stuckelberger, T. Nietzold, G. N. Hall, B. West, J. Werner, B. Niesen, C. Ballif, V. Rose, D. P. Fenning, M. I. Bertoni, *IEEE J. Photovoltaics* **2017**, *7*, 590.
- [25] X. Li, Y. Luo, M. V. Holt, Z. Cai, D. P. Fenning, *Chem. Mater.* **2019**, *31*, 2778.
- [26] Y. Luo, S. Gamliel, S. Nijem, S. Aharon, M. Holt, B. Stripe, V. Rose, M. I. Bertoni, L. Etgar, D. P. Fenning, *Chem. Mater.* **2016**, *28*, 6536.
- [27] R. L. Z. Hoyer, P. Schulz, L. T. Schelhas, A. M. Holder, K. H. Stone, J. D. Perkins, D. Vigil-Fowler, S. Siol, D. O. Scanlon, A. Zakutayev, A. Walsh, I. C. Smith, B. C. Melot, R. C. Kurchin, Y. Wang, J. Shi, F. C. Marques, J. J. Berry, W. Tumas, S. Lany, V. Stevanović, M. F. Toney, T. Buonassisi, *Chem. Mater.* **2017**, *29*, 1964.
- [28] P. Gratia, I. Zimmermann, P. Schouwink, J.-H. Yum, J.-N. Audinot, K. Sivula, T. Wirtz, M. K. Nazeeruddin, *ACS Energy Lett.* **2017**, *2*, 2686.
- [29] H. X. Dang, K. Wang, M. Ghasemi, M.-C. Tang, M. De Bastiani, E. Aydin, E. Duzon, D. Barrit, J. Peng, D.-M. Smilgies, S. De Wolf, A. Amassian, *Joule* **2019**, *3*, 1746.
- [30] P. E. Marchezi, E. M. Therézio, R. Szostak, H. C. Loureiro, K. Bruening, A. Gold-Parker, M. A. Melo, C. J. Tassone, H. C. Tolentino, M. F. Toney, *J. Mater. Chem. A* **2020**, *8*, 9302.
- [31] A. Al-Ashouri, E. Köhnen, B. Li, A. Magomedov, H. Hempel, P. Caprioglio, J. A. Márquez, A. B. M. Vilches, E. Kasparavicius, J. A. Smith, N. Phung, D. Menzel, M. Grischek, L. Kegelmann, D. Skroblin, C. Gollwitzer, T. Malinauskas, W. Jošt, G. Matič, B. Rech, R. Schlattmann, M. Topič, L. Korte, A. Abate, B. Stannowski, D. Neher, M. Stollerfoht, T. Unold, V. Getautis, S. Albrecht, *Science* **2020**, *370*, 1300.
- [32] T. J. Jacobsson, J.-P. Correa-Baena, M. Pazoki, M. Saliba, K. Schenk, M. Grätzel, A. Hagfeldt, *Energy Environ. Sci.* **2016**, *9*, 1706.
- [33] M. Saliba, T. Matsui, J.-Y. Seo, K. Domanski, J.-P. Correa-Baena, M. K. Nazeeruddin, S. M. Zakeeruddin, W. Tress, A. Abate, A. Hagfeldt, M. Grätzel, *Energy Environ. Sci.* **2016**, *9*, 1989.
- [34] T. A. S. Doherty, A. J. Winchester, S. Macpherson, D. N. Johnstone, V. Pareek, E. M. Tennyson, S. Kosar, F. U. Kosasih, M. Anaya, M. Abdi-Jalebi, Z. Andaji-Garmaroudi, E. L. Wong, J. Madéo, Y.-H. Chiang, J.-S. Park, Y.-K. Jung, C. E. Petoukhoff, G. Divitini, M. K. L. Man, C. Ducati, A. Walsh, P. A. Midgley, K. M. Dani, S. D. Stranks, *Nature* **2020**, *580*, 360.
- [35] S. Jariwala, H. Sun, G. W. P. Adhyaksa, A. Lof, L. A. Muscarella, B. Ehrlér, E. C. Garnett, D. S. Ginger, *Joule* **2019**, *3*, 3048.
- [36] W. Li, S. K. Yadavalli, D. Lizarazo-Ferro, M. Chen, Y. Zhou, N. P. Padture, R. Zia, *ACS Energy Lett.* **2018**, *3*, 2669.
- [37] T. W. Jones, A. Osherov, M. Alsari, M. Sponseller, B. C. Duck, Y.-K. Jung, C. Settens, F. Niroui, R. Brenes, C. V. Stan, Y. Li, M. Abdi-Jalebi, N. Tamura, J. E. Macdonald, M. Burghammer, R. H. Friend, V. Bulović, A. Walsh, G. J. Wilson, S. Lilliu, S. D. Stranks, *Energy Environ. Sci.* **2019**, *12*, 596.
- [38] T. A. S. Doherty, S. Nagane, D. J. Kubicki, Y.-K. Jung, D. N. Johnstone, A. N. Iqbal, D. Guo, K. Frohna, M. Danaie, E. M. Tennyson, S. Macpherson, A. Abfalterer, M. Anaya, Y.-H. Chiang, P. Crout, F. S. Ruggeri, S. M. Collins, C. P. Grey, A. Walsh, P. A. Midgley, S. D. Stranks, *Science* **2021**, *374*, 1598.
- [39] I. A. Ovid'ko, C. S. Pande, R. A. Masumura, in *Nanomaterials Handbook*, (Ed: Y. Gogotsi), CRC Press, Boca Raton, FL, USA **2006**, pp. 531–552.
- [40] A. M. Glazer, *Acta Crystallogr., Sect. B: Struct. Sci., Cryst. Eng. Mater.* **1972**, *28*, 3384.
- [41] P. A. Beckmann, *Cryst. Res. Technol.* **2010**, *45*, 455.
- [42] I. Mela, C. Poudel, M. Anaya, G. Delpont, K. Frohna, S. Macpherson, T. A. S. Doherty, A. Scheeder, S. D. Stranks, C. F. Kaminski, *Adv. Funct. Mater.* **2021**, *31*, 2100293.
- [43] K. Frohna, M. Anaya, S. Macpherson, J. Sung, T. A. S. Doherty, Y.-H. Chiang, A. J. Winchester, K. W. P. Orr, J. E. Parker, P. D. Quinn, K. M. Dani, A. Rao, S. D. Stranks, *Nat. Nanotechnol.* **2022**, *17*, 190.
- [44] K. P. McKenna, *ACS Energy Lett.* **2018**, *3*, 2663.
- [45] W. Li, M. U. Rothmann, Y. Zhu, W. Chen, C. Yang, Y. Yuan, Y. Y. Choo, X. Wen, Y.-B. Cheng, U. Bach, J. Etheridge, *Nat. Energy* **2021**, *6*, 624.
- [46] S. Macpherson, T. A. S. Doherty, A. J. Winchester, S. Kosar, D. N. Johnstone, Y.-H. Chiang, K. Galkowski, M. Anaya, K. Frohna, A. N. Iqbal, B. Roose, Z. Andaji-Garmaroudi, P. A. Midgley, K. M. Dani, S. D. Stranks, eprints, arXiv:2107.09549, **2021**.
- [47] Y.-H. Seo, J. H. Kim, D.-H. Kim, H.-S. Chung, S.-I. Na, *Nano Energy* **2020**, *77*, 105164.
- [48] P. A. Midgley, A. S. Eggeman, *IUCr* **2015**, *2*, 126.
- [49] R. F. Egerton, *Electron Energy-Loss Spectroscopy in the Electron Microscope*, Springer US, New York **2011**.

- [50] S. Svanström, A. G. Fernández, T. Sloboda, T. J. Jacobsson, H. Rensmo, U. B. Cappel, *Phys. Chem. Chem. Phys.* **2021**, *23*, 12479.
- [51] B. Chen, P. N. Rudd, S. Yang, Y. Yuan, J. Huang, *Chem. Soc. Rev.* **2019**, *48*, 3842.
- [52] N. Li, Y. Luo, Z. Chen, X. Niu, X. Zhang, J. Lu, R. Kumar, J. Jiang, H. Liu, X. Guo, B. Lai, G. Brocks, Q. Chen, S. Tao, D. P. Fenning, H. Zhou, *Joule* **2020**, *4*, 1743.
- [53] D. N. Johnstone, P. Crout, S. Høgås, B. Martineau, J. Laulainen, S. Smeets, S. Collins, E. Jacobsen, J. Morzy, E. Prestat, T. Doherty, T. Ostasevicius, H. W. Ánes, T. Bergh, R. Tovey, E. Opheim, *pyxem/pyxem: pyxem 0.12.0*, Zenodo, **2020**, <https://doi.org/10.5281/zenodo.3968871>.
- [54] M. Basham, J. Filik, M. T. Wharmby, P. C. Y. Chang, B. El Kassaby, M. Gerring, J. Aishima, K. Levik, B. C. A. Pulford, I. Sikharulidze, D. Sneddon, M. Webber, S. S. Dhesi, F. Maccherozzi, O. Svensson, S. Brockhauser, G. Náráy, A. W. Ashton, *J. Synchrotron Radiat.* **2015**, *22*, 853.
- [55] J. Zemann, *Acta Crystallogr.* **1965**, *18*, 139.
- [56] M. Lumbreras, J. Protas, S. Jebbari, G. J. Dirksen, J. Schoonman, *Solid State Ionics* **1986**, *20*, 295.